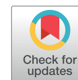

Self-inhibition effect of metal incorporation in nanoscaled semiconductors

Bin Zhu[a,b,1], Ding Yi[c,d,1], Yuxi Wang[a,b,1], Hongyu Sun[e], Gang Sha[f], Gong Zheng[f,g], Erik C. Garnett[e], Bozhi Tian[h], Feng Ding[c,i,2], and Jia Zhu[a,b,2]

[a]National Laboratory of Solid State Microstructures, College of Engineering and Applied Sciences, Nanjing University, Nanjing 210093, People's Republic of China; [b]Jiangsu Key Laboratory of Artificial Functional Materials, Nanjing University, Nanjing 210093, People's Republic of China; [c]Center for Multidimensional Carbon Materials (CMCM), Institute for Basic Science (IBS), Ulsan 44919, Republic of Korea; [d]Department of Physics, School of Science, Beijing Jiaotong University, Beijing 100044, People's Republic of China; [e]Center for Nanophotonics, Fundamental Research on Matter Institute for Atomic and Molecular Physics (AMOLF), 1098 XG Amsterdam, The Netherlands; [f]Herbert Gleiter Institute of Nanoscience, Nanjing University of Science and Technology, Nanjing 210094, People's Republic of China; [g]Ministry of Industry and Information Technology (MIIT) Key Laboratory of Advanced Metallic and Intermetallic Materials Technology, Nanjing University of Science and Technology, Nanjing 210094, People's Republic of China; [h]Department of Chemistry, The University of Chicago, Chicago, IL 60637; and [i]School of Materials Science and Engineering, Ulsan National Institute of Science and Technology (UNIST), Ulsan 44919, Republic of Korea

Edited by Peter J. Rossky, Rice University, Houston, TX, and approved December 13, 2020 (received for review May 25, 2020)

There has been a persistent effort to understand and control the incorporation of metal impurities in semiconductors at nanoscale, as it is important for semiconductor processing from growth, doping to making contact. Previously, the injection of metal atoms into nanoscaled semiconductor, with concentrations orders of magnitude higher than the equilibrium solid solubility, has been reported, which is often deemed to be detrimental. Here our theoretical exploration reveals that this colossal injection is because gold or aluminum atoms tend to substitute Si atoms and thus are not mobile in the lattice of Si. In contrast, the interstitial atoms in the Si lattice such as manganese (Mn) are expected to quickly diffuse out conveniently. Experimentally, we confirm the self-inhibition effect of Mn incorporation in nanoscaled silicon, as no metal atoms can be found in the body of silicon (below 10^{17} atoms per cm^{-3}) by careful three-dimensional atomic mappings using highly focused ultraviolet-laser-assisted atom-probe tomography. As a result of self-inhibition effect of metal incorporation, the corresponding field-effect devices demonstrate superior transport properties. This finding of self-inhibition effect provides a missing piece for understanding the metal incorporation in semiconductor at nanoscale, which is critical not only for growing nanoscale building blocks, but also for designing and processing metal–semiconductor structures and fine-tuning their properties at nanoscale.

semiconductor nanowires | self-inhibition effect | metal catalyst | density-functional theory calculation

The controlled incorporation of metal impurities in semiconductor at nanoscale is critical for various applications such as transistors, sensors, solar cells, catalysis, and batteries (1–15). However, the atomic behaviors of the metal incorporating processes have not been completely understood. Nanoscaled semiconductors, for example semiconductor nanowires, can be taken as a model example, in which the colossal injection of metal atoms has been widely reported (16–35). It was generally believed that the amount of metallic atom in semiconductor should be limited by the equilibrium solubility (36). However, it was found that gold (Au) was incorporated into the Si nanowires (Si NWs) with a concentration ranging from 10^{17} to 10^{20} atoms per cm^{-3} (37–39). Later, aluminum (Al) has also been detected in Si NWs with an extraordinarily high concentration (2×10^{20} – 2×10^{21} atoms per cm^{-3}), about four orders of magnitude higher than that of their equilibrium solubility (40). Therefore, how to understand and control the injection of metal atoms into semiconductor at nanoscale remains an open and critical challenge, especially as some incorporated metals (such as Au) serve as the deep-level impurity, detrimental to semiconductors (41, 42).

In this article, we reveal that the incorporation of metal atoms into semiconductor at nanoscale has strong dependence on metal types, where a Au or Al atom tends to substitute a Si atom and then tightly bond in the Si lattice, while a Mn or Mg atom behaves as an interstitial in the Si lattice and can easily diffuse out of the Si NW. Experimentally, we report that there is no injection of manganese (Mn) atoms into silicon NWs observed. After careful structural and elemental study of transmission electron microscopy (TEM), energy-dispersive X-ray analysis (EDX) and highly focused ultraviolet (UV)-laser-assisted atom-probe tomography (APT), no Mn signal was detected in the whole body of Si NWs. It is noted that rather than offering a competing methodology that replaces Au catalyst with Mn, here in this work we provide a fundamental understanding regarding the mechanism of metal incorporation into semiconductor at nanoscale. We first reveal the incorporation of metal atoms into semiconductor at nanoscale has strong dependence on metal types and the differences between self-inhibition effect of interstitial elements and substitution elements. Therefore, this finding, particularly the self-inhibition effect of interstitial elements, provides important guidelines for designing, growing, and

CHEMISTRY

Significance

Understanding and controlling the incorporation of metal into nanoscaled semiconductor is foundational for semiconductor processing. Through theoretical calculation and experimental results, we reveal that the interstitial atoms in the Si lattice such as Mn can quickly diffuse out of Si nanowires conveniently, thus can achieve high purity of Si nanowires. This finding of self-inhibition effect not only provides understanding of impurity incorporation at nanoscale, but also provides an extra knob for rational catalyst designs of nanoscale building blocks, and fine-tuning their electrical, optical, and thermal properties for various applications.

Author contributions: B.Z., F.D., and J.Z. designed research; B.Z., Y.W., H.S., and G.Z. performed research; B.Z., D.Y., G.S., E.C.G., B.T., and F.D. analyzed data; and B.Z., D.Y., F.D., and J.Z. wrote the paper.

The authors declare no competing interest.

This article is a PNAS Direct Submission.

Published under the PNAS license.

[1]B.Z., D.Y., and Y.W. contributed equally to this work.

[2]To whom correspondence may be addressed. Email: f.ding@unist.ac.kr or jiazhu@nju.edu.cn.

This article contains supporting information online at https://www.pnas.org/lookup/suppl/doi:10.1073/pnas.2010642118/-/DCSupplemental.

Published January 18, 2021.

Downloaded at AMOLF on January 20, 2021

processing metal–semiconductor structures and fine-tuning their properties at nanoscale.

In order to understand the underlying mechanism that governs the concentration of impurities in semiconductor NWs, we firstly explored the formation of six impurity atoms (Al, Au, Mn, Mg, B, and P) in a Si lattice (*SI Appendix*, sections A and B). It is found that for atoms such as Au, Al, B, and P, it is more energetically favorable for them to replace Si atoms in the lattice (Fig. 1*A*), while the formation of metal interstitials inside Si lattice is more favorable for Mn and Mg (Fig. 1*B*). The replaced Au or Al atom in the Si lattice is tightly embedded in the tetrahedral lattice and the formation energies of them are 1.11 and 1.02 eV, respectively (Fig. 1*D*). In contrast, the interstitial Mn or Mg atoms in the Si lattice are energetically less stable, with the formation energies up to 1.53 and 2.13 eV, respectively. The diffusion of the embedded Au or Al atom must go through a position-exchange mechanism and therefore the barriers are quite high, 2.70 and 3.40 eV, for Au and Al, respectively. As expected, the impurities like B and P are contained in the catalyst; they present even higher diffusion barriers (3.90 and 3.98 eV), which is why they serve as the common dopants (26). In sharp contrast, the diffusion barriers of the interstitial Mn and Mg in the Si lattice is as low as 0.67 and 1.01 eV (Fig. 1*D*), which means the fast diffusion of the Mn and Mg interstitials in Si lattice is expected at an elevated temperature.

The above results clearly demonstrate that, in comparison with the mostly used Au and Al catalyst, the Mn or Mg atom in Si lattice is highly unstable and they can easily diffuse out of the Si NW once they are embedded into the NW by chance during growth. To further understand the kinetics of their atomic incorporation into the Si NW during growth, we developed an impurity flow model (Fig. 1*C* and *SI Appendix*, section C) which predicted that, the concentration of the Mn in Si NW could be reduced to the level of 10^{-7} to 10^{-10} in a reasonable temperature range of Si NW growth (500–900 °C), which are 3–8 orders of magnitude lower than that of Au or Al in Si NW. We would like to note that the very low diffusion barrier of Mn and Mg also allows the radial diffusion of the incorporated metal atoms in the Si NW, which means the concentration of the Mg and Mn impurities in the Si NW can be further reduced either by thermal annealing during growth or postgrowth thermal treatment. Compared with Si, both B and P atoms are energetically more stable when incorporated into Si NW (Fig. 1 *E*, *Inset*), which means almost all B/P atoms will be found in Si NW after growth. Therefore, the concentration of B/P in the catalyst largely determines the final concentration of B/P in Si NW (26, 33).

To examine the above theoretical prediction, we experimentally prepared Mn-catalyzed Si NWs through a vapor transport process using the mixture of Si and Mn powders as sources(325 mesh, >99.99% purity, 20:1, wt./wt., 1,160 °C), commonly used

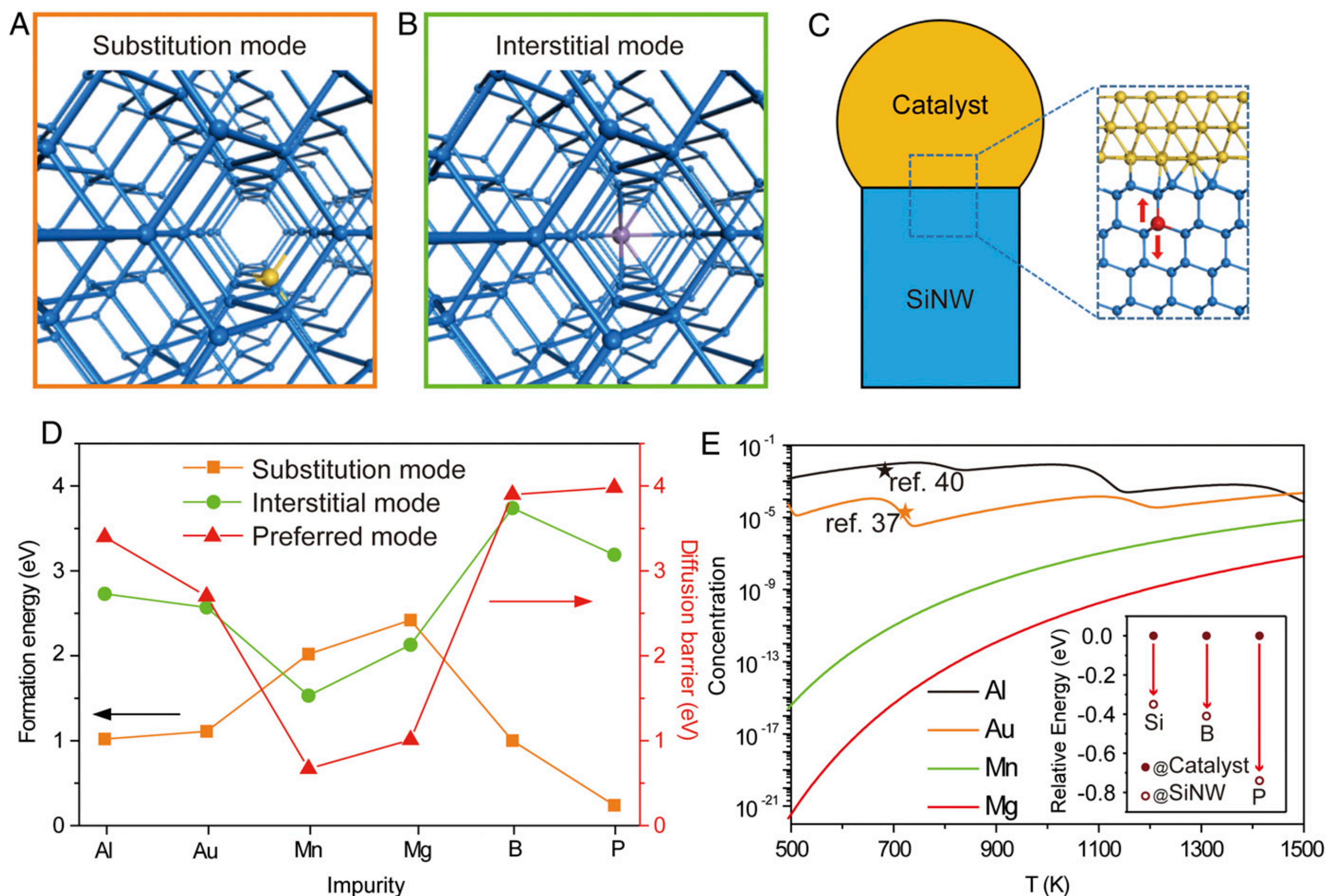

Fig. 1. Theoretical model of metal incorporation into the Si NW. Two typical structures of a metallic atom in Si lattice: (*A*) Substitution mode; (*B*) interstitial mode. Blue balls represent Si atoms while yellow and purple balls represent metallic atoms. (*C*) The atomic flow model near the metal–Si NW interface. The red ball represents the impurity. (*D*) Formation energies of substitution mode (orange line with square) and interstitial mode (green line with circle) of six different metal atoms in Si lattice, and the corresponding diffusion barriers in their preferred mode (red line with triangle). (*E*) Final concentration of Al, Au, Mn, and Mg atoms in the Si NW at the growth rate of 10 nm/s with respect to the temperature as predicted by our impurity flow model. Black and orange stars represent Al and Au concentration obtained in previous experiments. (*Inset*) Energy drops when Si, B, and P atoms are incorporated into Si NW from Au catalyst.

Downloaded at AMOLF on January 20, 2021

for various semiconductor NW growth (9, 35, 43–51) (see more details about growth conditions in *Materials and Methods* and *SI Appendix*, section E). As expected, silicon NWs with diameters around 40–100 nm and several micrometers long can be obtained, with metallic nanoparticles on the tip of NWs (Fig. 2), as a typical feature of NW growth.

The crystal quality and composition of produced Mn-catalyzed Si NWs are carefully examined by an aberration-corrected TEM. Fig. 2*A* shows a typical nanowire with a metallic particle (dark black) on the tip. A high-resolution TEM micrograph of the metallic particle (Fig. 2*B*) presents atomic planes separated by 0.34 nm, and the selected area electron diffraction (SAED) in the right reveals a typical square pattern, both corresponding to (110) planes of Mn_5Si_3. The EDX spectra taken from the metallic nanoparticle (Fig. 2*E*, *Inset*, red arrow and *SI Appendix*, Fig. S7) also confirm the existence of both Si and Mn. The high-resolution TEM image and SAED of the wire part away from the tip (Fig. 2*C* and *SI Appendix*, Fig. S8) indicate the successful growth of crystalline Si NWs along (110) direction with the (111) atomic planes (separation, 0.31 nm). No significant Mn signal was found in the EDX spectra of the Si NW (Fig. 2*F*), suggesting that the Mn concentration is less than the EDX detection limit (∼1 at. %). Scanning TEM (STEM) and corresponding EDX elemental mapping images (Fig. 2*D*) reveal that Mn can only be detected in the metallic nanoparticle. This result was also confirmed by EDX line scan (Fig. 2*G*), where Mn and Si coexist in the metallic particle and no Mn can be detected in the wire.

As highly focused UV-laser-assisted APT has been demonstrated as a powerful tool to quantify the composition in the NW with atomic-scale spatial resolution (theoretical sensitivity ∼1 atomic part per million) (26, 37, 40, 52, 53), we used it for a rigorous examination of Si and Mn concentrations in the obtained NWs. Fig. 2*H* displays a three-dimensional (3D) atom-by-atom map of the as-grown Si NW where Si and O atoms are represented by blue and red dots, respectively. Different from most if not all the previous study, APT analysis also did not find any signal of metal, in this case Mn, in the body of Si NWs, which indicates that there is no observed injection of Mn into Si NWs.

Fig. 3 presents more detailed results of the Si NW during APT analysis. The mass spectrum recorded during APT analysis (Fig. 3*A*) further illustrates that the Mn atom cannot be examined out in the Si NW. In other words, according to the background signal, the concentration of Mn in the NW is below $(1 \pm 0.5) \times 10^{17}$ atoms per cm^{-3} ($\sim 3 \times 10^{-4\%}$). Fig. 3*B* displays two projections of a 300-nm-long segment of Si NW delineated by an isoconcentration surface drawn at the 98 at. % Si level. Radial (X) and axial (Z) concentration profiles of the Si NW are presented in Fig. 3 *C* and *E*. Toward the radial direction, the O concentration gradually decreases from the surface of NW to isoconcentration surface while the Mn concentration remains

CHEMISTRY

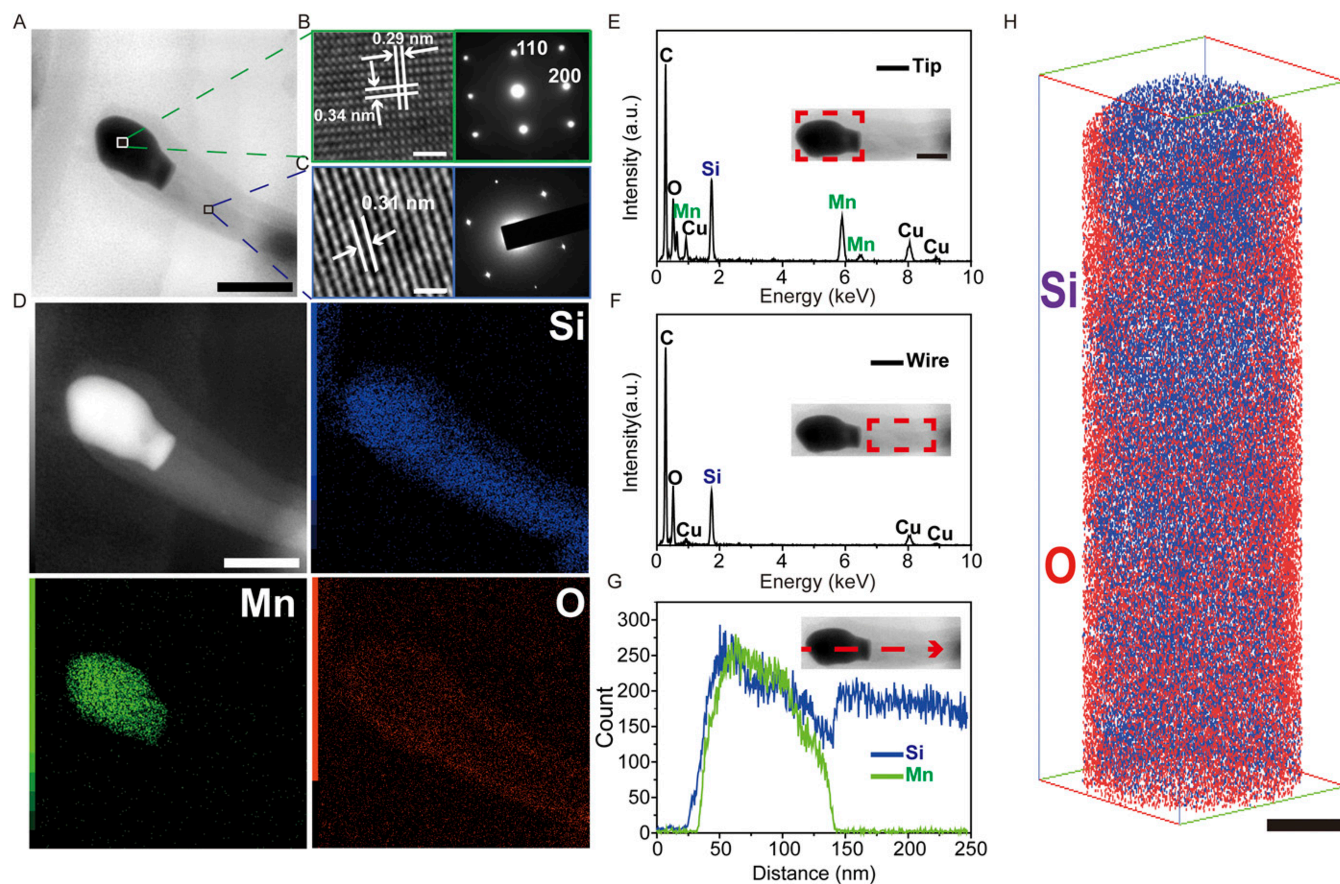

Fig. 2. Structural characterizations and elemental mapping of Mn-catalyzed Si NWs. (*A*) TEM image of the obtained NW. (Scale bar, 100 nm.) (*B*) HRTEM of the metallic particle (*Left*) (scale bar, 1 nm) and SAED pattern (*Right*). (*C*) HRTEM of the NW (*Left*) (scale bar, 1 nm) and SAED pattern (*Right*). (*D*) (*Top Left*) High-angle annular dark-field STEM image. (Scale bar, 100 nm.) Corresponding EDX elemental mapping images of the obtained NW. (*E*) EDX spectra of the tip (*Inset*, red dashed line part; scale bar, 50 nm). (*F*) EDX spectra of the wire (*Inset*, red dashed line part). (*G*) EDX line scan along the NW. (*H*) Three-dimensional APT atom-by-atom map of one portion of an NW. (Scale bar, 20 nm.) For clarity, only limited atoms are shown (3×10^4 atoms) and the reconstruction volume is $52 \times 52 \times 156$ nm^3.

Downloaded at AMOLF on January 20, 2021

https://doi.org/10.1073/pnas.2010642118

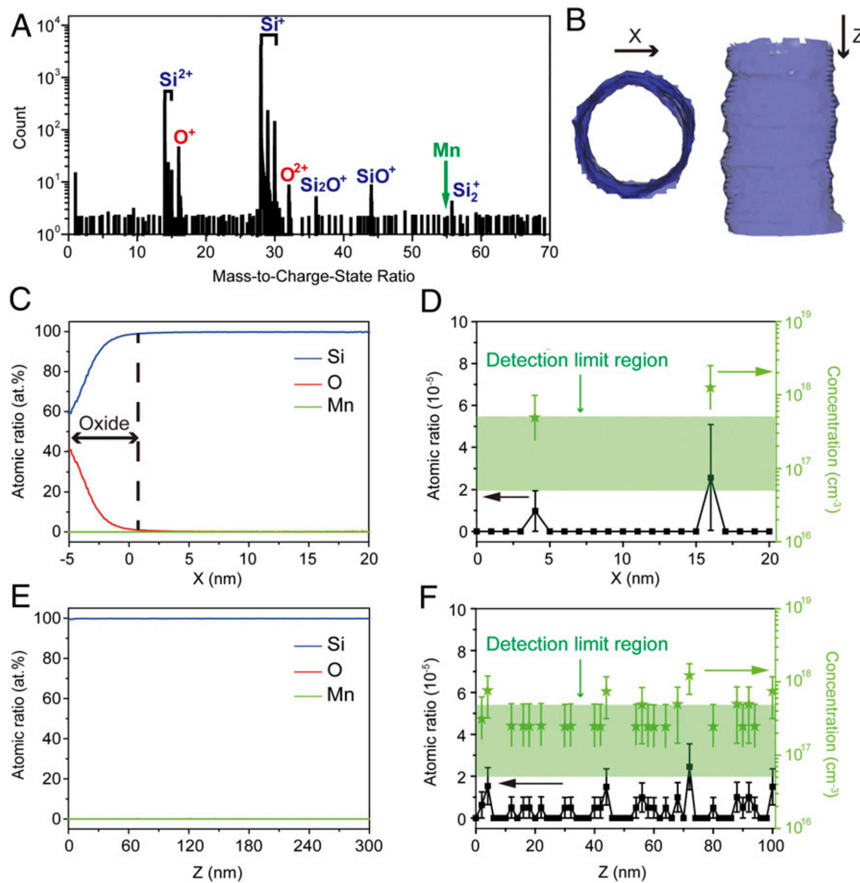

Fig. 3. APT data for Mn-catalyzed Si NWs. (*A*) A representative mass spectrum of the body part of Si NW recorded during UV-LEAP analysis. (*B*) Si 98 at. % isoconcentration surface of one portion of a NW: (*Left*) top view; (*Right*), side view. (*C* and *E*) Radial (*C*) and axial (*E*) concentration profiles of Si, O, and Mn in some parts of the NW. (*D* and *F*) Radial (*D*) and axial (*F*) concentration of Mn taken from parts of the measured NW. The green-shaded areas refer to the detection limit of APT. Error bars in *D* and *F* represent ±1 SD.

undetectable ($<3 \times 10^{-4\%}$) (Fig. 3*C*). For clarity, Fig. 3*D* presents the concentration of Mn separately in which the most atomic ratio values from APT were zero, suggesting the actual Mn concentration in the NW is below the detection limit of APT [green-shaded region in the Fig. 3*D*, $(2.75 \pm 2.25) \times 10^{17}$ atoms per cm^{-3}]. This is also consistent with the axial profiles of the Si NW (Fig. 3*E*), where along 300-nm-long NW, no Mn signal can be detected. It is observed that most concentration values of Mn locate in the detection limit region of APT, as shown in Fig. 3*F*, illustrating that there is no Mn detected. Compared to the reported results before (*SI Appendix*, Table S5), this distinct discovery illustrates that incorporation mechanism of Mn into Si NWs during growth is drastically different for those previously reported.

To probe the electrical transport properties of as-grown Mn-catalyzed Si NWs, field-effect transistors (FETs) were configured through depositing Si NWs on Si wafer with a top layer of 285-nm-thick silicon oxide (*SI Appendix*, Fig. S9). Fig. 4*A* shows the linear behavior in the source–drain current (I_{ds}) as a function of bias (V_{ds}) of a typical Mn-catalyzed Si NW device, suggesting good ohmic contacts. The dependence of I_{ds} on V_{ds} curves shows that the conductance increases as V_g increases, a characteristic of n-channel FET for Mn-catalyzed Si NW. The mobility of carriers

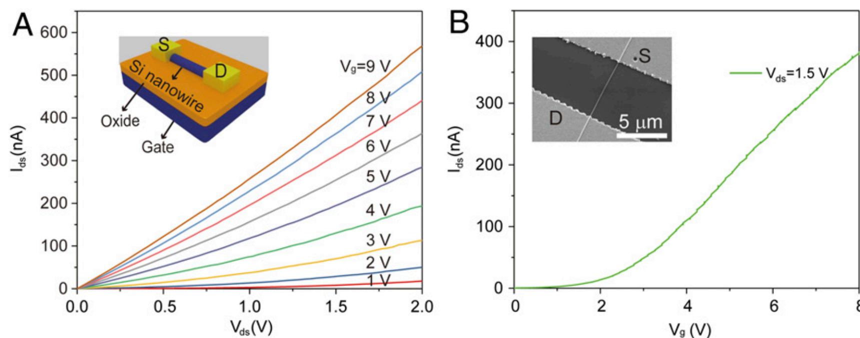

Fig. 4. Room-temperature mobility of Mn-catalyzed Si NWs FETs. (*A*) I_{ds} vs. V_{ds} measured on the Mn-catalyzed Si NW. (*Inset*) Schematic of the device structure and optical microscopy image of the device. (*B*) Typical I_{ds} vs. V_g curves of Mn-catalyzed Si NW. (*Inset*) SEM image of the FET device.

Downloaded at AMOLF on January 20, 2021

can be extracted from the transconductance based on dependence of I_{ds} on V_g (*Materials and Methods*). It is calculated that the Mn-catalyzed Si NWs yield mobility of ~30 cm^2/V s, a high value without any extra treatment or surface passivation (Fig. 4*B*). We made similar measurements on over 20 devices of Mn-catalyzed Si NWs to avoid systematic error. The statistical results (*SI Appendix*, Fig. S10) clearly show that the averaged mobility of Mn-catalyzed Si NWs reaches 58 cm^2/V s. Therefore, high quality of Mn-catalyzed Si NW is confirmed.

In summary, it is found that the injections of metal into nanoscaled semiconductors have strong dependence on metal types. Different from colossal injection behaviors of substitutional-type metals such as Au or Al that were previously reported, interstitial-type metals such as Mn or Mg have the self-inhibited incorporation. This effect of self-inhibition of metal incorporation is supported by both theoretical model and 3D atomic probe. Therefore, this finding provides the missing piece toward understanding metal incorporation behaviors into semiconductor at nanoscale, and opens up opportunities for designing and processing nanoscaled metal–semiconductor structures and devices.

Materials and Methods

To grow Mn-catalyzed Si NWs, the mixture of Si and Mn powders (325 mesh, >99.99% purity, 20:1, wt./wt.) was in the middle of a furnace tube where the temperature was 1,160 °C. The temperature of the substrate was about 700 °C. As carrier gas, 10% hydrogen in argon was used to protect the reaction from oxygen and its rate remained constant (60 sccm). The partial pressure was held at ~1,000 Pa during growth.

The morphology of Si NWs was characterized using a scanning electron microscope (SEM; Hitachi S-4800), TEM (JEM-2010, 200 kV), and a JEOL JEM-F200 equipped with energy dispersive X-ray spectroscopy and SAED. We use an UV-laser-assisted LEAP (local electrode atom probe) tomography (LEAP4000XSi, Cameca). The 3D reconstructions and statistical analysis of concentration frequency were performed using Cameca's IVAS program. For the preparation of NW APT specimens, we used the focused ion beam-based damage-free methodology to attach individual NWs to the top of a tungsten (W) support tip (*SI Appendix*, section F).

Back-gated FETs were fabricated on Si substrate with 285-nm oxide layer. Electron-beam lithography was used to write metal contact on individual Si NW for two-terminal FETs. The native oxide layer of Si nanowires was removed by HF dip (2 wt. %). As contact metal, 20 nm Pd and 60 nm Au was deposited by electron beam evaporation. A home-built system with <1-pA noise was used to measure electrical property. We used the transconductance value to estimate the mobility of carriers (54) according to the equation below:

$$dI/dV_g = m(C/L^2)V_{ds},$$

where μ is the carrier mobility, C is the capacitance, and L is the length of the Si NW (~8 μm). The Si NW capacitance is given by $C = 2\pi\varepsilon\varepsilon_o L/\ln(2\,h/r)$, where ε is the dielectric constant of SiO_2 (~4.5), h is the thickness of the silicon oxide layer (285 nm), and r is the Si NW radius (~40 nm).

First-principles calculations were performed by using the density-functional theory method implemented in the Vienna Ab initio Simulation Package (55, 56). The exchange-correlation potential was approximated by the generalized gradient approximation using the Perdew–Burke–Ernzerhof-type functional (57). The projector-augmented-wave (58) method, as well as a fixed plane-wave energy cutoff of 400 eV, was used in all calculations. For supercells with different shapes or sizes, the spacing of Monkhorst–Pack k-point sampling around 0.03 $Å^{-1}$ along each reciprocal lattice vector in the Brillouin zone was adopted. The climbing-image nudged elastic band method (59) was used for calculating the diffusion barriers. The convergence of energy and force were set as 10^{-4} eV and 10^{-2} eV·$Å^{-1}$, respectively.

Data Availability. All study data are included in the article and/or *SI Appendix*.

ACKNOWLEDGMENTS. We acknowledge the microfabrication center of National Laboratory of Solid State Microstructures for technique support. Prof. Jia Zhu acknowledges the support from the XPLORER PRIZE. This work is jointly supported by grants from the National Key Research and Development Program of China (2017YFA0205700), National Natural Science Foundation of China (52002168, 12022403, 51925204, 11874211, and 61735008), Natural Science Foundation of Jiangsu Province (BK20190311), Key Science and Technology Inovation Program of Shandong Province (2019JZZY020704), and the Fundamental Research Funds for the Central Universities (021314380140 and 021314380150). F.D. acknowledges the support of the Institute for Basic Science (IBS-R019-D1) of Korea. E.C.G. and H.S. were supported by the Dutch Science Foundation through the Joint Solar Program III.

1. J. Goldberger, A. Hochbaum, R. Fan, P. Yang, Silicon vertically integrated nanowire field effect transistors. *Nano Lett.* **6**, 973–977 (2006).
2. J. Xiang *et al*., Ge/Si nanowire heterostructures as high-performance field-effect transistors. *Nature* **441**, 489–493 (2006).
3. Y. Cui, Q. Wei, H. Park, C. M. Lieber, Nanowire nanosensors for highly sensitive and selective detection of biological and chemical species. *Science* **293**, 1289–1292 (2001).
4. B. Tian *et al*., Coaxial silicon nanowires as solar cells and nanoelectronic power sources. *Nature* **449**, 885–889 (2007).
5. C. K. Chan *et al*., High-performance lithium battery anodes using silicon nanowires. *Nat. Nanotechnol.* **3**, 31–35 (2008).
6. H. Yan *et al*., Programmable nanowire circuits for nanoprocessors. *Nature* **470**, 240–244 (2011).
7. Z. L. Wang, J. Song, Piezoelectric nanogenerators based on zinc oxide nanowire arrays. *Science* **312**, 242–246 (2006).
8. N. A. Melosh *et al*., Ultrahigh-density nanowire lattices and circuits. *Science* **300**, 112–115 (2003).
9. M. H. Huang *et al*., Room-temperature ultraviolet nanowire nanolasers. *Science* **292**, 1897–1899 (2001).
10. M. C. McAlpine, H. Ahmad, D. Wang, J. R. Heath, Highly ordered nanowire arrays on plastic substrates for ultrasensitive flexible chemical sensors. *Nat. Mater.* **6**, 379–384 (2007).
11. J. Wallentin *et al*., InP nanowire array solar cells achieving 13.8% efficiency by exceeding the ray optics limit. *Science* **339**, 1057–1060 (2013).
12. S. A. Mann *et al*., Quantifying losses and thermodynamic limits in nanophotonic solar cells. *Nat. Nanotechnol.* **11**, 1071–1075 (2016).
13. P. Xie, Q. Xiong, Y. Fang, Q. Qing, C. M. Lieber, Local electrical potential detection of DNA by nanowire-nanopore sensors. *Nat. Nanotechnol.* **7**, 119–125 (2011).
14. S. Kim *et al*., Designing morphology in epitaxial silicon nanowires: The role of gold, surface chemistry, and phosphorus doping. *ACS Nano* **11**, 4453–4462 (2017).
15. C. W. Pinion, D. P. Nenon, J. D. Christesen, J. F. Cahoon, Identifying crystallization- and incorporation-limited regimes during vapor-liquid-solid growth of Si nanowires. *ACS Nano* **8**, 6081–6088 (2014).
16. J. Johansson *et al*., Structural properties of <111>B -oriented III-V nanowires. *Nat. Mater.* **5**, 574–580 (2006).
17. M. J. Bierman, Y. K. Lau, A. V. Kvit, A. L. Schmitt, S. Jin, Dislocation-driven nanowire growth and Eshelby twist. *Science* **320**, 1060–1063 (2008).
18. F. Panciera *et al*., Synthesis of nanostructures in nanowires using sequential catalyst reactions. *Nat. Mater.* **14**, 820–825 (2015).
19. R. Zhang, Y. Lifshitz, S. Lee, Oxide-assisted growth of semiconducting nanowires. *Adv. Mater.* **15**, 635–640 (2003).
20. D. D. D. Ma, C. S. Lee, F. C. K. Au, S. Y. Tong, S. T. Lee, Small-diameter silicon nanowire surfaces. *Science* **299**, 1874–1877 (2003).
21. Y. Cui, C. M. Lieber, Functional nanoscale electronic devices assembled using silicon nanowire building blocks. *Science* **291**, 851–853 (2001).
22. Y. Su *et al*., Single-nanowire photoelectrochemistry. *Nat. Nanotechnol.* **11**, 609–612 (2016).
23. M. Heurlin *et al*., Continuous gas-phase synthesis of nanowires with tunable properties. *Nature* **492**, 90–94 (2012).
24. D. Jacobsson *et al*., Interface dynamics and crystal phase switching in GaAs nanowires. *Nature* **531**, 317–322 (2016).
25. J. C. Ho *et al*., Controlled nanoscale doping of semiconductors via molecular monolayers. *Nat. Mater.* **7**, 62–67 (2008).
26. D. E. Perea *et al*., Direct measurement of dopant distribution in an individual vapour-liquid-solid nanowire. *Nat. Nanotechnol.* **4**, 315–319 (2009).
27. C. Yang, Z. Zhong, C. M. Lieber, Encoding electronic properties by synthesis of axial modulation-doped silicon nanowires. *Science* **310**, 1304–1307 (2005).
28. J. Zhu *et al*., Formation of chiral branched nanowires by the Eshelby Twist. *Nat. Nanotechnol.* **3**, 477–481 (2008).
29. P. V. Radovanovic, C. J. Barrelet, S. Gradecak, F. Qian, C. M. Lieber, General synthesis of manganese-doped II-VI and III-V semiconductor nanowires. *Nano Lett.* **5**, 1407–1411 (2005).
30. C. Thelander *et al*., Nanowire-based one-dimensional electronics. *Mater. Today* **9**, 28–35 (2006).
31. S. Hoffmann *et al*., Axial p-n junctions realized in silicon nanowires by ion implantation. *Nano Lett.* **9**, 1341–1344 (2009).
32. M. D. Kelzenberg *et al*., Enhanced absorption and carrier collection in Si wire arrays for photovoltaic applications. *Nat. Mater.* **9**, 239–244 (2010).
33. Y. Cui, L. J. Lauhon, M. S. Gudiksen, J. Wang, C. M. Lieber, Diameter-controlled synthesis of single-crystal silicon nanowires. *Appl. Phys. Lett.* **78**, 2214 (2001).
34. M. S. Gudiksen, C. M. Lieber, Diameter-selective synthesis of semiconductor nanowires. *J. Am. Chem. Soc.* **122**, 8801–8802 (2000).

Downloaded at AMOLF on January 20, 2021

35. A. M. Morales, C. M. Lieber, A laser ablation method for the synthesis of crystalline semiconductor nanowires. *Science* **279**, 208–211 (1998).
36. F. A. Trumbore, Solid solubilities of impurity elements in germanium and silicon. *Bell Syst. Tech. J.* **30**, 205–233 (1960).
37. J. E. Allen *et al*., High-resolution detection of Au catalyst atoms in Si nanowires. *Nat. Nanotechnol.* **3**, 168–173 (2008).
38. J. B. Hannon, S. Kodambaka, F. M. Ross, R. M. Tromp, The influence of the surface migration of gold on the growth of silicon nanowires. *Nature* **440**, 69–71 (2006).
39. S. H. Oh *et al*., Point defect configurations of supersaturated Au atoms inside Si nanowires. *Nano Lett.* **8**, 1016–1019 (2008).
40. O. Moutanabbir *et al*., Colossal injection of catalyst atoms into silicon nanowires. *Nature* **496**, 78–82 (2013).
41. C. B. Collins, R. O. Carlson, C. J. Gallagher, Properties of gold-doped silicon. *Pyhs. Rev.* **105**, 1168–1173 (1957).
42. G. J. Fairfield, J. M. Fairfield, Diffusion of gold into silicon crystals. *J. Electrochem. Soc.* **112**, 200–203 (1965).
43. D. Yu *et al*., Nanoscale silicon wires synthesized using simple physical evaporation. *Appl. Phys. Lett.* **72**, 3458 (1998).
44. Z. W. Pan, Z. R. Dai, Z. L. Wang, Nanobelts of semiconducting oxides. *Science* **291**, 1947–1949 (2001).
45. J. M. Higgins, A. L. Schmitt, I. A. Guzei, S. Jin, Higher manganese silicide nanowires of Nowotny chimney ladder phase. *J. Am. Chem. Soc.* **130**, 16086–16094 (2008).
46. D. Seo *et al*., Structural modulation of silicon nanowires by combining a high gas flow rate with metal catalysts. *Nanoscale Res. Lett.* **10**, 190 (2015).
47. F. Martelli *et al*., Manganese-induced growth of GaAs nanowires. *Nano Lett.* **6**, 2130–2134 (2006).
48. L. Güniat, P. Caroff, A. Fontcuberta I Morral, Vapor phase growth of semiconductor nanowires: Key developments and open questions. *Chem. Rev.* **119**, 8958–8971 (2019).
49. N. Shin, M. Chi, M. A. Filler, Sidewall morphology-dependent formation of multiple twins in Si nanowires. *ACS Nano* **7**, 8206–8213 (2013).
50. S. V. Sivaram, H. Y. Hui, M. de la Mata, J. Arbiol, M. A. Filler, Surface hydrogen enables subeutectic vapor-liquid-solid semiconductor nanowire growth. *Nano Lett.* **16**, 6717–6723 (2016).
51. M. Ek, M. A. Filler, Atomic-scale choreography of vapor-liquid-solid nanowire growth. *Acc. Chem. Res.* **51**, 118–126 (2018).
52. W. Chen *et al*., Incorporation and redistribution of impurities into silicon nanowires during metal-particle-assisted growth. *Nat. Commun.* **5**, 4134 (2014).
53. O. Moutanabbir, D. Isheim, D. N. Seidman, Y. Kawamura, K. M. Itoh, Ultraviolet-laser atom-probe tomographic three-dimensional atom-by-atom mapping of isotopically modulated Si nanoscopic layers. *Appl. Phys. Lett.* **98**, 013111 (2011).
54. D. R. Khanal, J. Wu, Gate coupling and charge distribution in nanowire field effect transistors. *Nano Lett.* **7**, 2778–2783 (2007).
55. G. Kresse, J. Furthmüller, Efficiency of ab-initio total energy calculations for metals and semiconductors using a plane-wave basis set. *Comput. Mater. Sci.* **6**, 15–50 (1996).
56. G. Kresse, J. Furthmüller, Self-interaction correction to density functional approximation for many electron systems. *Phys. Rev. B Condens. Matter* **54**, 11169–11186 (1996).
57. J. P. Perdew, K. Burke, M. Ernzerhof, Generalized gradient approximation made simple. *Phys. Rev. Lett.* **77**, 3865–3868 (1996).
58. P. E. Blöchl, Projector augmented-wave method. *Phys. Rev. B Condens. Matter* **50**, 17953–17979 (1994).
59. G. Henkelman, B. P. Uberuaga, H. Jónsson, A climbing image nudged elastic band method for finding saddle points and minimum energy paths. *J. Chem. Phys.* **113**, 9901 (2000).

Downloaded at AMOLF on January 20, 2021